Geophysical Journal International

Geophys. J. Int. (2023) **235,** 1725–1735
Advance Access publication 2023 August 31
GJI Seismology

https://doi.org/10.1093/gji/ggad329

Reproducing complex anisotropy patterns at subduction zones from splitting intensity analysis and anisotropy tomography

Judith M. Confal [1], Paola Baccheschi,[2] Silvia Pondrelli,[1] Foivos Karakostas [1], Brandon P. VanderBeek [3], Zhouchuan Huang[4] and Manuele Faccenda[3]

[1] *Istituto Nazionale di Geofisica e Vulcanologia, Sezione di Bologna,* 40127 *Bologna, Italy. E-mail: judithconfal@gmail.com*
[2] *Istituto Nazionale di Geofisica e Vulcanologia, Sezione di Roma,* 00143, *Roma, Italy*
[3] *Dipartimento di Geoscienze, Università di Padova,* 35131, *Padua, Italy*
[4] *Department of Earth and Planetary Science,* 210023, *School of Earth Sciences and Engineering, Nanjing University, Nanjing, China*

Accepted 2023 August 15. Received 2023 May 22; in original form 2023 February 1

SUMMARY

Measurements of seismic anisotropy provide a lot of information on the deformation and structure as well as flows of the Earth's interior, in particular of the upper mantle. Even though the strong and heterogeneous seismic anisotropic nature of the upper mantle has been demonstrated by a wealth of theoretical and observational approaches , most of standard teleseismic body-wave tomography studies overlook *P*- and *S*-wave anisotropy, thus producing artefacts in tomographic models in terms of amplitude and localization of heterogeneities. Conventional methods of seismic anisotropy measurement have their limitations regarding lateral and mainly depth resolution. To overcome this problem much effort has been done to develop tomographic methods to invert shear wave splitting data for anisotropic structures, based on finite-frequency sensitivity kernels that relate model perturbations to splitting observations. A promising approach to image the upper mantle anisotropy is the inversion of splitting intensity (SI). This seismic observable is a measure of the amount of energy on the transverse component waveform and, to a first order, it is linearly related to the elastic perturbations of the medium through the 3-D sensitivity kernels, that can be therefore inverted, allowing a high-resolution image of the upper mantle anisotropy. Here we present an application of the SI tomography to a synthetic subduction setting. Starting from synthetic SKS waveforms, we first derived high-quality SKS SI measurements; then we used the SI data as input into tomographic inversion. This approach enables high-resolution tomographic images of upper-mantle anisotropy through recovering vertical and lateral changes in anisotropy and represents a propaedeutic step to the real cases of subduction settings. Additionally this study was able to detect regions of strong dipping anisotropy by allowing a 360° periodic dependence of the splitting vector.

Key words: Tomography; Seismic anisotropy; Subduction zone processes.

INTRODUCTION

Subduction environments are known for their complex and strong anisotropy, especially in the upper mantle. Many synthetic models (e.g. Faccenda & Capitanio 2013; Confal *et al.* 2018) and some observational studies (e.g. Long & Silver 2009) identify trench perpendicular backarc anisotropy, subslab trench parallel anisotropy, and circular anisotropic patterns around the edges of a retreating slab, while within the inner portions of the subduction zone and close to the slab the anisotropy patterns reflect the poloidal component of mantle flow excited by subduction. Most body-wave tomography studies still assume an isotropic upper mantle, which could lead to artefacts being mapped in the tomographic images. Few studies tried to correct isotropic velocities with known anisotropy from SKS splitting measurements (O'Driscoll *et al.* 2011; Confal *et al.* 2020). In such models anisotropy is assumed to be uniformly distributed with depth or the velocities are corrected with anisotropy from synthetic models (Bezada *et al.* 2016; Confal *et al.* 2020), with the limit of not representing the whole complexity of the tectonic evolution of a region. Directly inverting for anisotropy and isotropic velocities (e.g. Eberhart-Phillips & Reyners 2009; Wang & Zhao 2013; Wei *et al.* 2019; Rappisi *et al.* 2022) causes usually a loss in resolution, due to additional unknowns in the inversion and ray coverage.

Seismic anisotropy measurements can be obtained with several methods that may detect anisotropy at different depths depending on the characteristics of the used seismic waves. Especially in regard to lateral and vertical resolution, most methods which retrieve

© The Author(s) 2023. Published by Oxford University Press on behalf of The Royal Astronomical Society. This is an Open Access article distributed under the terms of the Creative Commons Attribution License (http://creativecommons.org/licenses/by/4.0/), which permits unrestricted reuse, distribution, and reproduction in any medium, provided the original work is properly cited.

Downloaded from https://academic.oup.com/gji/article/235/2/1725/7257552 by University of Padua: Biblioteca sc. statistiche user on 05 September 2023

anisotropic parameters from SKS real data have clear and well known limits (i.e. near vertical incidence angle) and often should be combined with other observables (e.g. different phases) and explicit consideration of finite frequency effects approximated via Fresnel zones to get a broader understanding. Surface waves detect depth dependent azimuthal and radial anisotropy originating in the uppermost mantle (e.g. Montagner 2002), while Pn-tomography is limited to the mantle immediately below the Moho (e.g. Hearn 1996; Diaz *et al.* 2013). For both surface waves and Pn studies the results are seismic anisotropy vectors, reported on regular grids, with a resolution strictly related to waveform lengths, usually good to be compared with global (Kustowski *et al.* 2008 and references therein) or regional studies (e.g. Zhu *et al.* 2015), but sometimes poor for smaller areas (e.g. Fry *et al.* 2010). The most commonly used method to detect anisotropy is shear wave splitting analysis, which gives, for each single station-event pair, two splitting parameters: the fast polarization direction (FPD) and the delay time (TD) between fast and slow split waves. In particular, shear-wave splitting (SWS) analyses that use P-to-S converted phases at the core–mantle boundary (e.g. PKS, SKS, SKKS and so on) are widely applied as a powerful tool to investigate the mantle structure and flow as well as diverse geometry of subduction zones. However, splitting measurements retrieve anisotropic properties of the whole medium crossed by a seismic ray from the base of the mantle to the surface, lacking a vertical resolution to define the distribution of the anisotropy with depth (e.g. Silver & Chan 1991; Savage 1999). Perturbations of elastic parameters are difficult to retrieve since splitting parameters do not accumulate linearly along the ray path and the weight of anisotropy close to the receiver side is larger (e.g. Saltzer *et al.* 2000).

Another method to obtain seismic anisotropy data is to measure the splitting intensity (SI). This parameter was first studied by Chevrot (2000) and represents the relative difference between the amplitude of transverse and radial components. SI builds up linearly along the path of the ray (Silver & Long 2011), at least in low frequency ranges (Chevrot *et al.* 2004), and therefore can be used in tomographic inversions. Indeed, fast polarization direction and time delay can be determined fitting the azimuthal variation of SI with a sine function, with amplitude and phase shift related to delay time and fast velocity direction, respectively (Chevrot 2000; Kong *et al.* 2015). Therefore, an inversion method has been designed to invert SI measurements to recover vertical and lateral changes in anisotropy (e.g. Chevrot 2006; Monteiller & Chevrot 2011).

Other tomographic approaches to retrieve anisotropic parameters of the upper mantle, like full-waveform inversion (e.g. Lin *et al*. 2014a; Beller & Chevrot 2020), from teleseismic *P* waves (e.g. VanderBeek & Faccenda 2021) or theoretically from direct *S* waves, receive attention recently. A combination of waveforms, and especially including *P* waveforms, would improve the recovery of orientations of anisotropic fabric (Beller & Chevrot 2020), but it is still computationally very expensive and needs a very good data coverage. However, in this study we decided to continue exploring the possibilities of retrieving anisotropy from SKS on the basis of SI measurements because it is an already established approach for real data cases (e.g. Monteiller & Chevrot 2011; Huang & Chevrot 2021). The reason for using SKS instead of *S* is that in reality direct *S* waves have a contribution of source side anisotropy unknown while the polarization of SKS waves is known. In this study, we use the available velocity distribution, including anisotropy, of a synthetic subducting slab model designed by VanderBeek & Faccenda (2021) (Figs 1, S1 and S2) to determine SI values from SKS waves and obtain the corresponding splitting parameters. We then invert obtained SI values to produce an anisotropic tomography model that allowed us to test how much of the original heterogeneous anisotropic pattern can be recovered with our workflow.

Synthetic model and data

The synthetic model for this study comes from an anisotropic petrological-thermomechanical model of a subducting slab (Faccenda 2014) used by VanderBeek & Faccenda (2021) to test the possibility of retrieving upper mantle anisotropy in complex systems with teleseismic *P* waves. The slab, with a half width of 1000 km and a thickness of 90 km at the surface, subducted freely for about 20 Ma and stagnated at the 660 km discontinuity. The slab gets progressively thinner by thermal erosion as it subducts. The anisotropic time dependent fabric (Kaminski *et al*. 2004; Faccenda & Capitanio 2013) accounts for brittle deformation as well as dislocation, diffusion and creep mechanisms (VanderBeek & Faccenda 2021). The main anisotropic simulated patterns are: (1) frozen anisotropy in the slab; (2) anisotropy from entrained mantle flow parallel to the subducting slab; (3) toroidal anisotropic pattern at the edges of the slab in the upper 300 km and (4) trench-parallel anisotropy beneath the plate (Fig. 1). The elastic tensors have been simplified with only hexagonal symmetry. As a reference 1-D model VanderBeek & Faccenda (2021) used IASP91 Kennett & Engdahl (1991). Within this model synthetic seismograms have been computed with SPECFEM3D as recorded by a regular grid network of 770 stations with 75 km spacing (Fig. S3). In this paper, we use the synthetics SKS waveforms computed for eight events with a magnitude of 6.5, a dominant period of 15 s, at a hypocentral depth of 50 km, evenly distributed in backazimuth (each 45°) and with an epicentral distance of 120° from the middle of study (Fig. 1 this study; VanderBeek & Faccenda 2021). Although the distribution of backazimuths are ideal compared to real data cases, the distribution of incidence angles is limited to 4.5°–7.5°, due to identical epicentral distances of the synthetic events. This becomes especially evident at 0° latitude (Fig. S4) with only about 0.8° varying incidence angles.

SI measurements

SI represents the amount of energy on the transverse component of a seismic waveform, when it passes through an anisotropic medium (Chevrot 2000). The strength of SI is directly related to the backazimuth, and therefore fast polarization direction and time delay can be determined by fitting the azimuthal variation of splitting intensities with a sine function, with amplitude and phase shift corresponding to delay time and fast velocity direction, respectively (e.g. Chevrot 2000; Favier & Chevrot 2003).

In this study, we used a modification of a Fortran program by Kong *et al.* (2015), to calculate splitting intensities and automatized it, to handle the large amount of data. First, the synthetic data are filtered with a bandpass filter between 10 and 40 s and through a Hanning window; then the mean and trend are removed (e.g. Goldstein & Snoke 2005; Kong *et al.* 2015). The horizontal components are rotated into the radial and transverse components. A time window of 5 s before and 20 s after the SKS arrival and a dominant period of 15 s ($\tau = 30$ s) for the Wiener filter have been used, following the known characteristics of the synthetic waveforms. Using a Wiener filter with a pre-described frequency standardizes the waveforms and reduces the variations of apparent splitting (Monteiller & Chevrot 2010). Afterwards the transverse component T projected onto the derivative of the radial component R' equals the SI (Chevrot 2000;

Downloaded from https://academic.oup.com/gji/article/235/2/1725/7257552 by University of Padua: Biblioteca sc. statistiche user on 05 September 2023

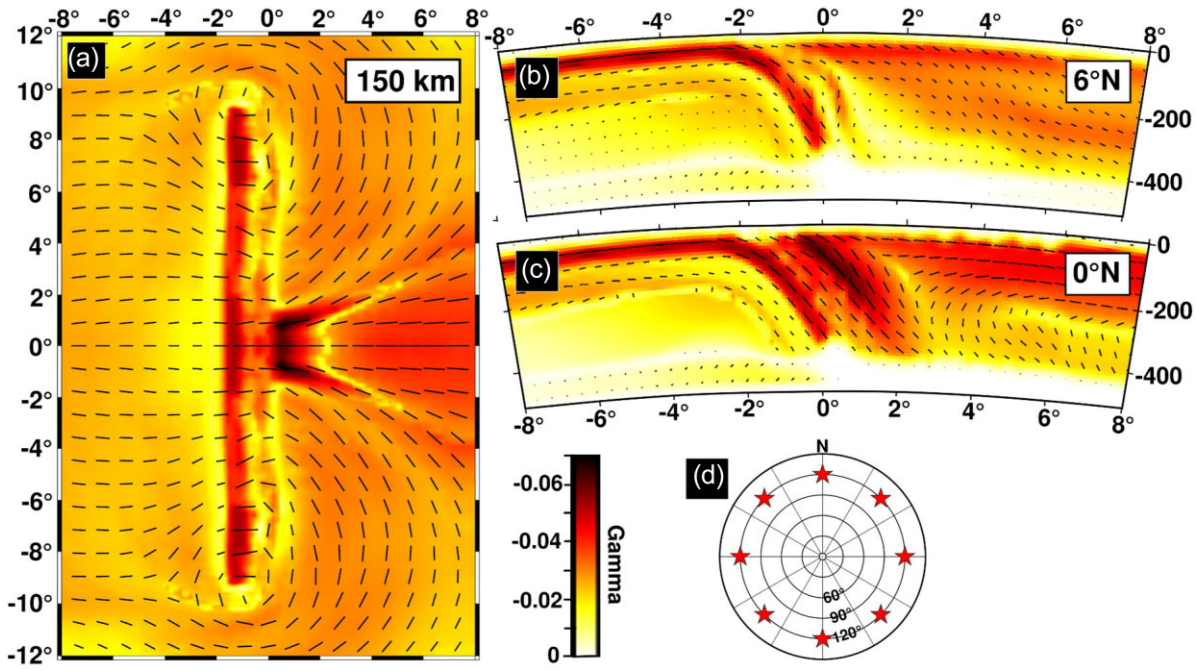

Figure 1. Horizontal (a) and vertical (b, c) cross sections through the true anisotropy of the synthetic model by VanderBeek & Faccenda (2021), plotted with gamma and azimuth (a) and azimuth-scaled dip (b, c) marked with black sticks (reduced amount of nodes). In (d) the eight event locations, used in this study, are marked with red stars, where the centre represents 0°N/0°E in the model.

Monteiller & Chevrot 2010)

$$\mathrm{SI} = 2\frac{\int T(t)\,R'(t)\,\mathrm{d}t}{\int R'(t)^2\mathrm{d}t}. \tag{1}$$

A bootstrap method has been used to calculate the standard deviation of SI representing its error (after e.g. Efron & Tibshirani 1986; Kong *et al.* 2015)

$$\sigma\sqrt{\sum\left(T(t)+\frac{\mathrm{SI}*R'(t)}{2}\right)^2}. \tag{2}$$

Following the dependence of SI from a sinusoidal distribution with backazimuth, we fit the sinusoidal curve

$$C = a_1\cos(2x) + a_2\sin(2x) + a_3\cos(x) + a_4\sin(x) \tag{3}$$

with an unknown vector a_n and x as the evenly spaced backazimuths, that best fit the eight SI values for each station (Fig. 2). The first two summands describe a curve with 180° periodicity, while the whole formula describes a curve with 360° periodicity (green and purple curves, respectively, in the example on the right-hand side of Fig. 2). This approach is reliable in this test, where a backazimuthal homogeneity is guaranteed by the evenly distribution of events.

SI and backazimuth (BAZ) of each event are weighted with an error (σ). With a singular value decomposition of a matrix consisting of

$$Y_1 = \cos(2*\mathrm{BAZ}),\ Y_2 = \sin(2*\mathrm{BAZ}),\ Y_3 = \cos(\mathrm{BAZ}),$$
$$Y_4 = \sin(\mathrm{BAZ}) \tag{4}$$

and SI values, a least square solution to define a_n can be found (see Chevrot 2000 for further descriptions).

Only Y_1 and Y_2 are used to fit the 180° periodic curve (green curves in Figs 2 and 3), where the amplitude of the sinusoidal curve represents the time delay δt_1 and the phase corresponds to the fast polarization direction ϕ_1 (Chevrot 2000), which can be seen as equivalent to splitting parameters retrieved from traditional shear wave splitting for a single station:

$$\delta t_1 = \sqrt{(a_1)^2+(a_2)^2},\ \delta t_2 = \sqrt{(a_3)^2+(a_4)^2} \tag{5}$$

$$\phi_1 = 0.5\tan^{-1}\left(\frac{-a_1}{a_2}\right),\ \phi_2 = 0.5\tan^{-1}\left(\frac{-a_3}{a_4}\right). \tag{6}$$

Taking into account that the original model has dipping anisotropy that usually is not detected by common methods to measure shear wave splitting or spitting intensity, we tried to identify the presence of any pattern in SI distribution with backazimuth for stations located over dipping anisotropy with respect to those located over horizontal anisotropy (e.g. Chevrot & van der Hilst 2003; Monteiller & Chevrot 2010, 2011; Romanowicz & Yuan 2012). Chevrot (2000) showed that for simple one layer models it is possible to identify dips that are larger than 30°. A symmetry break in the 360° periodic sinusoidal curve results in two different amplitudes (purple curves in Figs 2 and 3). For the least square solution Y_1, Y_2, Y_3 and Y_4 are used and two sets of splitting parameters δt_1, δt_2, ϕ_1 and ϕ_2 can be calculated and a high δt_2 can be seen as an indicator for a dipping structure.

Horizontal average anisotropy results

The computational process of calculating SI values for all available synthetics events and fitting them with 180° oscillating sinusoidal curves has been repeated over all the 770 stations and results are shown in Fig. 2 on the left-hand side.

Splitting parameters calculated from SI show high time delays (~1.5–2.5 s) in the backarc region, perpendicular to the

Downloaded from https://academic.oup.com/gji/article/235/2/1725/7257552 by University of Padua: Biblioteca sc. statistiche user on 05 September 2023

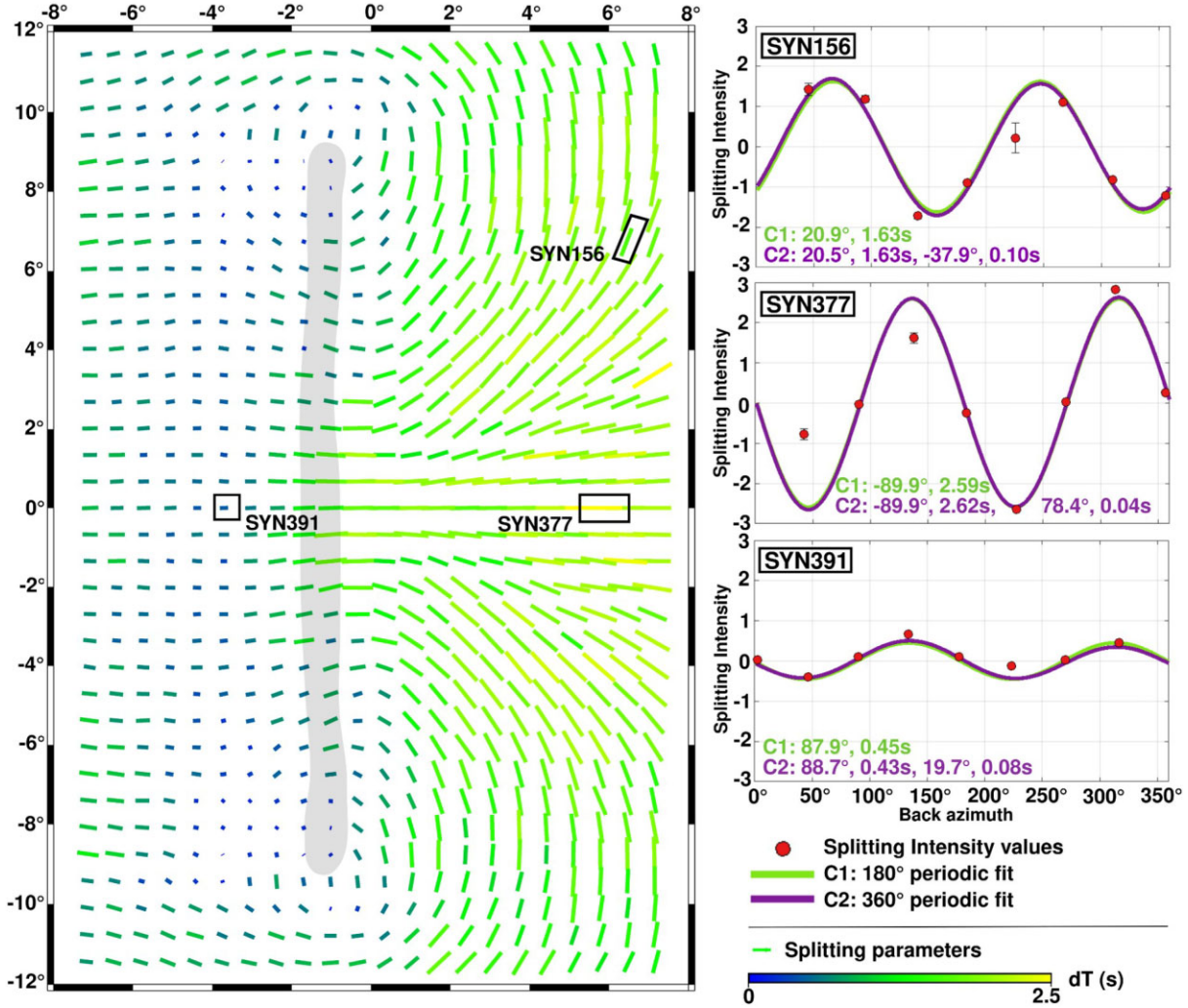

Figure 2. On the left-hand side, shear wave splitting parameters at the 770 stations with directions of vectors representing the fast polarization direction and the length and colour depending on the time delay. The grey transparent shape represents the outline of the slab at 150 km depth (Fig. 1a). The figures on the right-hand side represent the 180° and 360° oscillating sinusoidal curves at three stations (respectively green, C1 and purple, C2) and their respective splitting intensity values (red dots). Green numbers represent δt_1 and ϕ_1 values for the 180° fitting curve and purple values represent δt_1, ϕ_1, δt_2 and ϕ_2 values for the 360° periodic fitting curve.

trench, evolving into a circular pattern towards the edges of the slab. Below the slab, time delays are much smaller (0.2–1 s) and mostly trench perpendicular, except the circular pattern around the edges.

In comparison with the anisotropy from the original model, the SI method recovers well the apparent horizontal single layer anisotropy, for example around the edges of the slab and in the backarc region far from the slab. Below the slab, west of the slab, in the model (Fig. S2) there is a trench perpendicular pattern in the top layer (down to 200 km) and a trench parallel pattern with weaker anisotropy below it. Since the two perpendicular patterns cancel each other out, very small values of time delays are detected (e.g. Fig. 2, SYN391) and only the direction of the shallower but stronger anisotropic layer is recovered (top 150 km of the model). Single SI measurements at each station show mostly a very good fit with the 180° periodic curve (e.g. green curves on the right-hand side of Fig. 2), especially in areas with simple horizontal or slightly dipping anisotropy, as seen for example in the backarc area (e.g. Fig. 2, SYN377) and around the slab (e.g. Fig. 2, SYN156).

Dipping anisotropy results

The well recovered horizontal anisotropy is however an apparent anisotropy that could not distinguish the presence of multilayer or dipping anisotropy. Nevertheless we have observed that at some stations the SI measurements do not fit very well a 180° oscillating curve with two maxima at the same height (e.g. green curves in Fig. 3, SYN387). On the contrary, when fitting a 360° periodic curve (purple curve), which allows different amplitudes within the 360° backazimuthal range, the fit improves. Chevrot (2000) described this phenomenon as related to the presence of one single layer of dipping anisotropy; however, it seems to be still difficult to pin this variation to a pattern, mainly in real data (Montellier & Chevrot 2010), even though a mathematical explanation has been found (Romanowicz & Yuan 2012).

In this study, we test this theory for the complex anisotropy patterns of the synthetic subduction model (Fig. S5), that is closer to a real distribution of anisotropy at depth with respect to a single layer anisotropy model. An evaluation of δt_2 for all the 770 stations is shown in Fig. 3(a), where it is evident that the sharpest boundary is

Downloaded from https://academic.oup.com/gji/article/235/2/1725/7257552 by University of Padua: Biblioteca sc. statistiche user on 05 September 2023

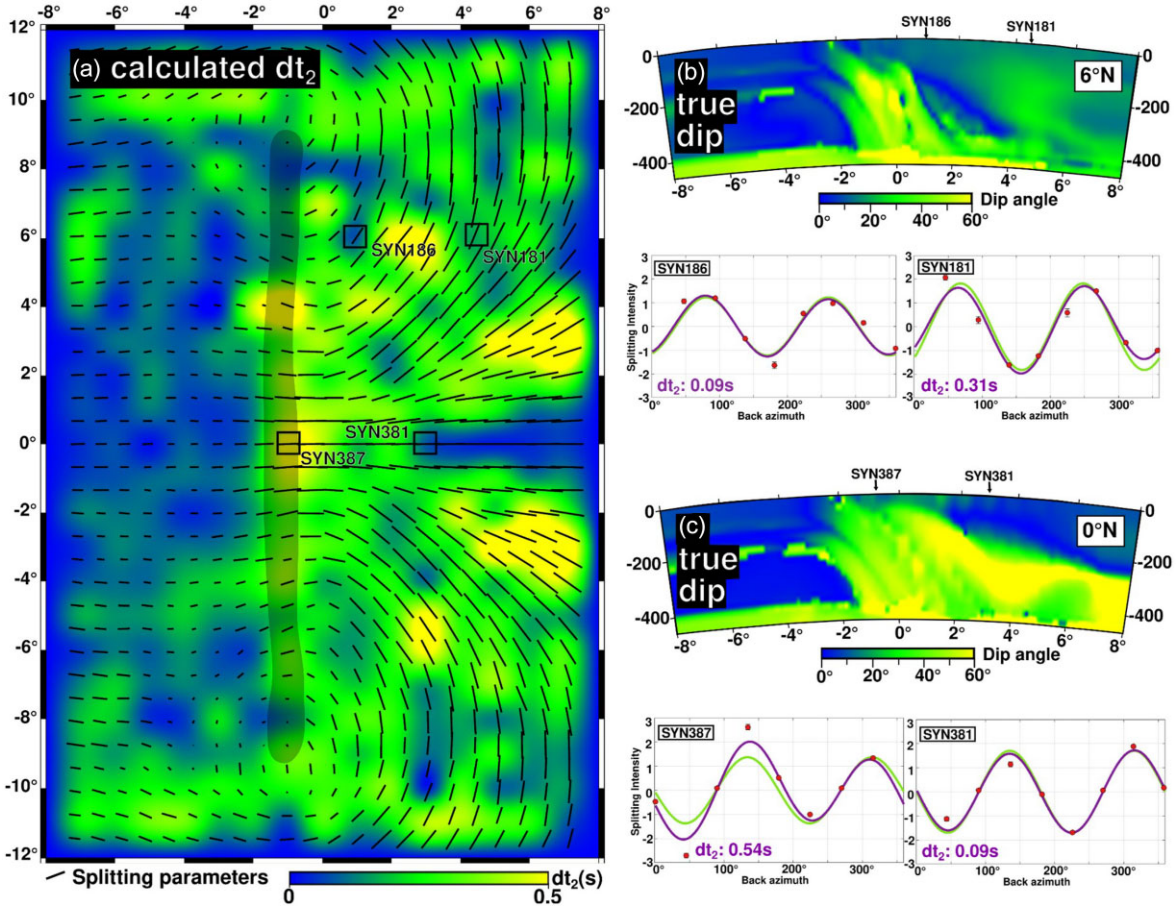

Figure 3. (a) Interpolation of calculated δt_2 values over the study area. The grey transparent shape represents the outline of the slab at 150 km depth (Fig. 1a). Panels (b) and (c) are true anisotropy directions on cross-sections of interpolated dip angles at 0°N and 6°N, respectively. Beneath (b) and (c) two examples of sinusoidal curves of calculated SI values are shown; their locations are indicated on (a) and on the true anisotropy cross sections. The legend for the sinusoidal curves is the same as in Fig. 2.

the trench. On the left part of the model, west of the trench, beneath the oceanic plate and where horizontal anisotropy prevails, δt_2 values are low (0–0.2 s, blue parts of Fig. 3a). Moving to the eastern part of the model, where dipping anisotropy is largely diffused at depth, δt_2 is high (Fig. 3a). It increases between $-2°$ and $-1°$ of longitude and between $-5°$ and $5°$ of latitude (0.4–0.6 s), which corresponds to the location of the slab at depths (e.g. Fig. 3, SYN387). The backarc area, in the centre of the slab (0° latitude), shows very small δt_2 values, but it increases again towards the edges of the slab, with some patches reaching maximum values, up to 0.7 s. Regions with vertical or nearly vertical anisotropy (backarc region at 0°N, e.g. Fig. 3, SYN381), as well as small dip angles (lower than 30°, e.g. SYN186) do not show an increase of δt_2, as already verified in theoretical studies (Chevrot 2000; Romanowicz & Yuan 2012). On the other hand, if there is a layer of dipping anisotropy (∼45°) with small strength beneath 200 km depth overlain by strong horizontal anisotropy (e.g. eastern part of 2°–4° latitude cross sections, Fig. S5), δt_2 values are very high. Thus, the dipping layer at great depth could influence the periodicity of the sinusoidal curve. However we should take into account that also the change from purely trench perpendicular to circular orientation could contribute with its complexity to this local high δt_2. The far northern and southern borders of the model present high δt_2 values in some areas as well, but they are certainly related to some boundary issues of the model, visible also in the fit of the curves of some boundary stations.

Inversion of SI

The most adopted method to quantify the anisotropy is to measure, on the individual SKS or SKKS waves, the two anisotropic splitting parameters DT and FPD , which describe a uniform layer of anisotropy beneath the station. This simple assumption draws the link between the description of the spatial variation of anisotropy and the anisotropic properties of the rock not directly, because the splitting parameters vary as a function of the angle between the azimuth of the fast axis and the backazimuth, leading thus to map an 'apparent' fast direction and delay time that has been interpreted as vertical variation of anisotropy. This is the case, for example, when a double layer structure shows a $\pi/2$ periodicity in traditional shear wave splitting (Silver & Savage 1994). To overcome this misinterpretation, many efforts have been made in recent years to develop methods that are able to accurately define the distribution of anisotropy through depth and most of them are based on the tomographic inversion of SI data rather than the traditional SKS or SKKS splitting measurements (e.g. Monteiller & Chevrot 2011; Huang & Chevrot 2021). Indeed, the nature of SKS or SKKS waves characterized by very poor vertical resolution due to the quasi vertical incidence angle (and the difficulty in separating the contributions from different segments of a ray path), makes it difficult to relate the splitting parameters to the effectively anisotropic perturbation of elastic parameters, severely hindering any tomographic approach

Downloaded from https://academic.oup.com/gji/article/235/2/1725/7257552 by University of Padua: Biblioteca sc. statistiche user on 05 September 2023

to imaging the mantle anisotropy. Also, the direct inversion of the SKS splitting measurements is impossible because splitting parameters are not obtained by a simple integration of seismic anisotropy along the ray path. On the contrary, the peculiar characteristic of the SI measurements make this observable tomographically invertible, since they accumulate linearly along the ray (Silver & Long 2011), thus allowing to overcome the problem of uncertainty of the distribution of seismic anisotropy in the upper mantle at different depths. Here, we have the unique opportunity to know *a priori* the geometry of a subduction zone and its pattern of anisotropy and we thus directly test the ability of SI tomography in replicating the anisotropic heterogeneities through depth. This test is propaedeutic for applying this approach to the real data.

There exists a wealth of literature describing the theoretical formulation of the anisotropic tomographic inversion using the SI parameter, among the others Favier & Chevrot (2003), Chevrot (2006), Monteiller & Chevrot (2011) and Mondal & Long (2019). In practice, $\gamma_c = \gamma \cos 2\varphi$ and $\gamma_s = \gamma \sin 2\varphi$ are the only two parameters to which SI is related (Favier & Chevrot 2003). φ is the azimuth of the projection of the symmetry axis on the horizontal plane and γ (gamma) is a dimensionless parameter representing the strength of shear wave anisotropy (Favier & Chevrot 2003; Becker *et al.* 2006; Chevrot 2006; Monteiller & Chevrot 2011; Lin *et al.* 2014a). This approach is possible if we assume that the dip has little effect on SKS and SKKS waves due to their nearly vertical propagation in those depths (Chevrot & Van der Hilst 2003). The tomographic problem to be solved consists in finding the 3-D distribution of an anisotropy vector, defined by its projections γ_c and γ_s on a geographical reference frame. In this paper, we invert the SI measurements, obtained from the synthetic waveforms, using the algorithm of Huang & Chevrot (2021), that allows the recovery of the horizontal anisotropy distribution. The SI kernels are computed choosing a lateral and vertical grid spacing of 0.1° and 5 km, respectively. The chosen parametrization allowed us to capture subwavelength anisotropic heterogeneities. In computing the 3-D kernel of SI we cannot completely rule out the effect of the shallower layer to anisotropy the anisotropy, including thus the near and mid-terms of SKS splitting. Indeed, as shown in Favier & Chevrot (2003) and in Lin *et al.* (2014b), the near and mid-field terms of SKS splitting should be properly considered, since they could affect the pattern of the sensitivity around the crustal discontinuity and have a significant contribution to the shear wave splitting intensities. For the synthetic study area, we parametrized the model choosing a 3-D grid node between 50 and 350 km depth, and with 0.5° grid spacing in horizontal planes and 10 km grid spacing in depth. We also choose the depth interval between the Moho depth (about 50 km) and 350 km depth considering that the main anisotropic source is located within the upper mantle at about 150–200 km depth. The tomographic inversion approach assumes a homogeneous background velocity model in the upper mantle. This assumption leads to neglect the curvature of SKS rays between 50 and 350 km depth (Monteiller & Chevrot 2011) and this artefact may introduce additional modelling error in the inversion that however does not affect the inversion because it is small compared to the general errors of SI measurements.

To stabilize the inversion process, damping and smoothing parameters have been applied, selected empirically by running a series of inversions with different damping and smoothing values. A damping of 10 and a smoothing of 200 have been selected after plotting the typical L-shape (Hansen 1992) trade-off curves of data variance versus model variance for each iteration (Fig. 4).

After inversion for the optimal model, the data residuals reduce by 84 per cent, from 1.02 to 0.41.

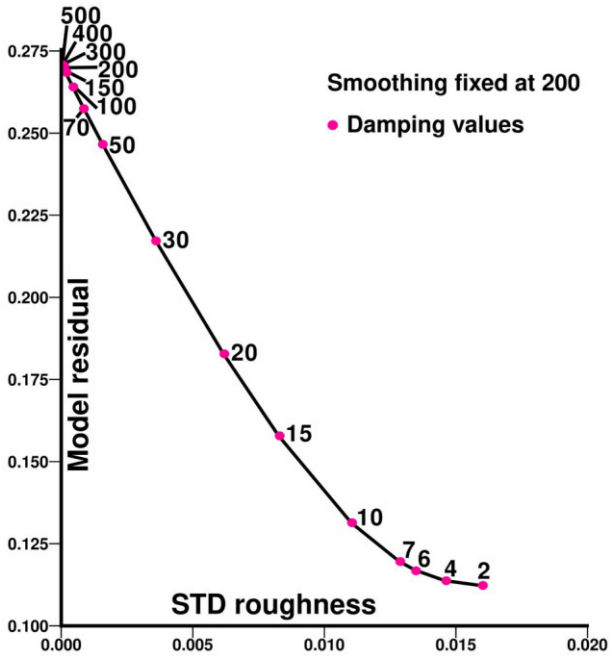

Figure 4. L-shaped trade-off curve of data misfit versus model roughness for different values of damping parameters with a fixed smoothing of 200.

In Fig. 5 the results obtained after the tomographic inversion are shown. Before discussing the results, it is worth noting that the inversion for anisotropy highlights a strong sensitivity to the lateral resolution and a relatively good vertical resolution. The layered anisotropy revealed by the tomographic inversion allows us to discuss some constraints on the depth variation and localization of the source of anisotropy. At first glance we observe that the pattern of fast directions and gamma are quite in agreement with the pattern of the anisotropy of the original synthetic subduction model. The most dominant and well reproduced feature is the circular pattern recognizable symmetrically around the northern and southern edge of the slab and comparable to the distribution of the model (Fig. S1). This feature is more prominent with increasing depth, reaching its best visibility between 150 and 250 km depth. In the mantle wedge, at approximately 4° and 6° and −4° and −6° of longitude and −1°/1° of latitude, a change in the fast axes could be recognized. Here, fast axes are oriented N–S at shallower layers and down to 100 km depth, while they seem to disappear at deeper layers in the mantle wedge. A more scattered distribution of fast axes is also present in the foreland region at 100 km depth, while moving to the deeper layers the pattern seems to be better organized. In the left part, west of the slab, an EW largely diffused direction is recovered in the shallower layer remaining even at depth, but weaker and more scattered.

In the upper mantle a strong anisotropy, thus high values of gamma, is present in the mantle wedge and in the backarc region and extended continuously from 50 to 350 km depth.

To assess the reliability of the tomographic model and estimate the horizontal and vertical resolution of the anisotropic model, we follow the approach of Huang & Chevrot (2021), performing two synthetic tests, both using the same parametrization applied for the optimal model inversion. In the first test (Synth-I), the anisotropic model from the inversion is used as the input model to compute the synthetic splitting intensities. The obtained synthetic data are then inverted for the input model. The synthetics test shows that the

Downloaded from https://academic.oup.com/gji/article/235/2/1725/7257552 by University of Padua: Biblioteca sc. statistiche user on 05 September 2023

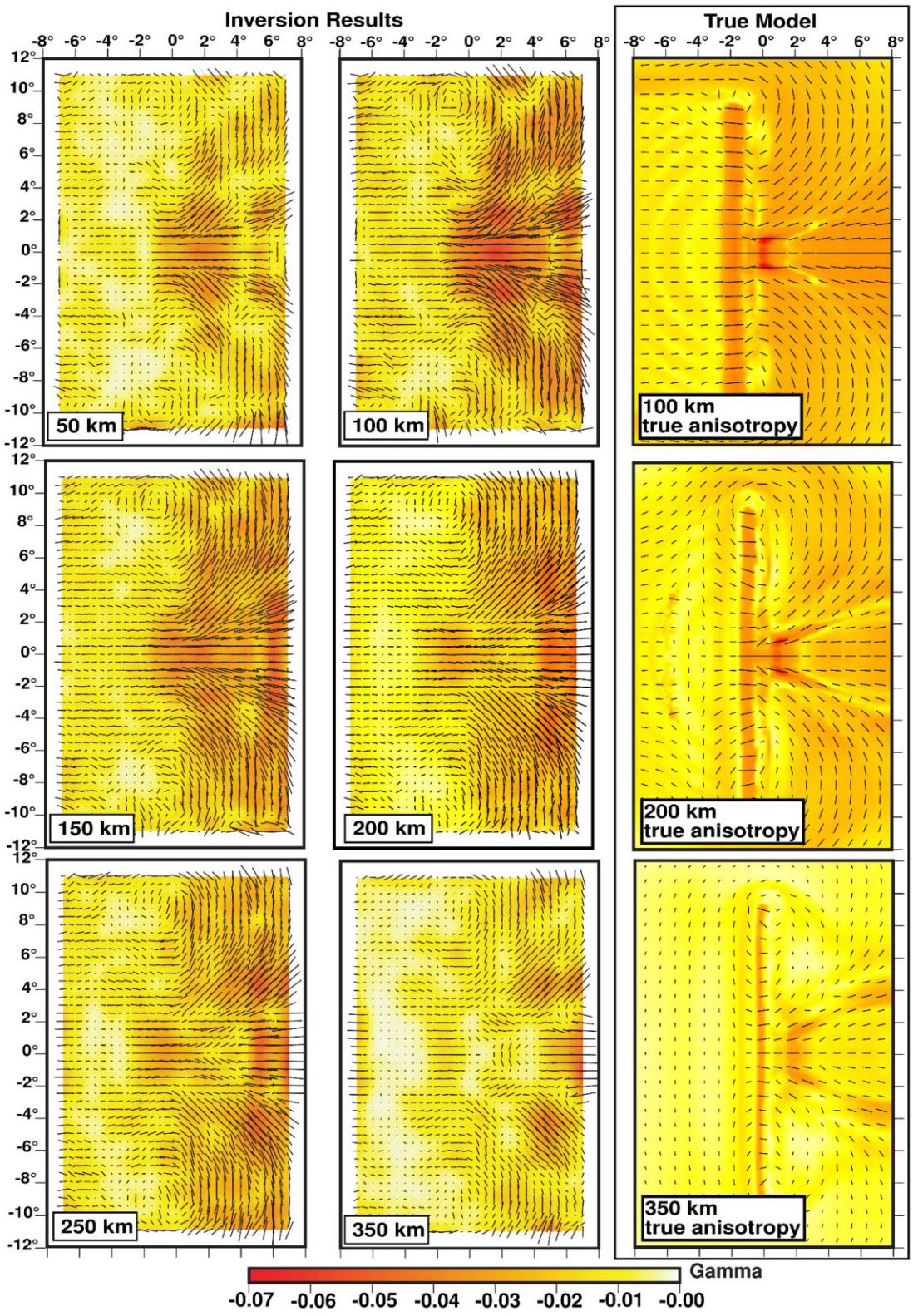

Figure 5. On the left-hand side the shear wave anisotropy inverted from the splitting intensity measurements at different depths. On the right-hand side, the true anisotropy of the model. The black bars represent the shear wave anisotropy, directed with azimuth of the fast axis φ and with the length proportional with γ (Gamma), the strength of the anisotropy also reported through the colour scale.

Downloaded from https://academic.oup.com/gji/article/235/2/1725/7257552 by University of Padua: Biblioteca sc. statistiche user on 05 September 2023

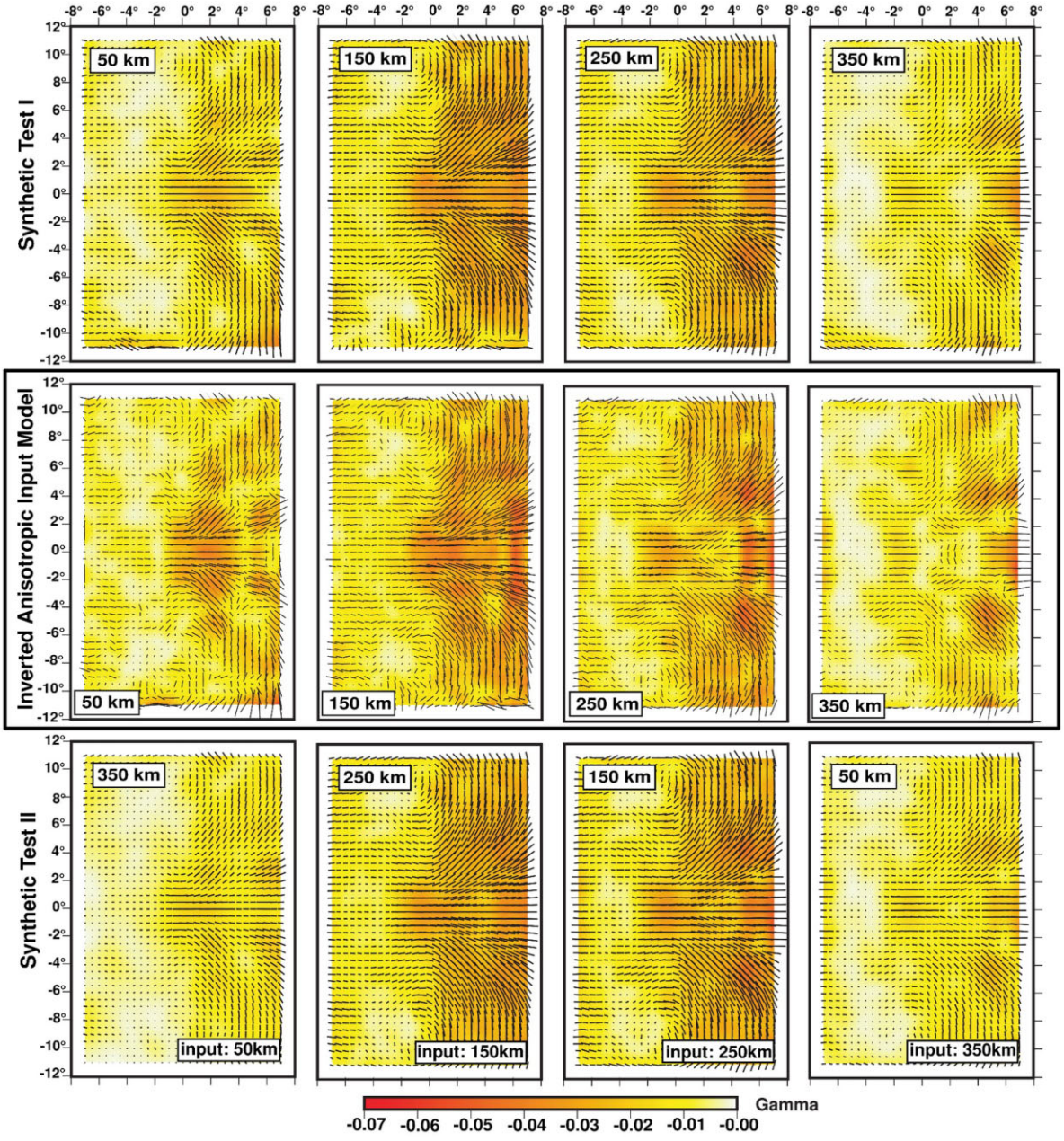

Figure 6. Results of synthetic tests. In the top row the inverted SKS-wave anisotropy is used as the input model, while in the lower test the depth slices of the inverted SKS-wave anisotropy are swapped vertically (after Huang & Chevrot 2021). The middle row represents the inverted anisotropic input model for both tests and corresponds to inversion results (Fig. 5).

inverted results (Fig. 6) are quite similar to the optimal anisotropic model, and the fast direction and patches of high and low intensity of anisotropy are correctly retrieved. In the second test (Synth-II), the optimal anisotropic model is swapped vertically, so that the anisotropic model at 50, 100, 150, 180, 250 and 350 km depths are used as the input models at 350, 250, 180, 150, 100 and 50 km depths, respectively. In the second synthetic test the anisotropic variations in terms of gamma and fast axes are still correctly retrieved with a good lateral resolution and a smaller vertical one.

We also recalculated the synthetics shear wave splitting from the optimal model (Fig. 7, red bars). The comparison with the shear wave splitting measurements of the sinusoidal curve fitting (Fig. 2 and blue bars in Fig. 7) shows a well recovery of the first-order pattern of measurements. In particular, the circular pattern of fast direction at the edges of the slab is perfectly recovered, as well as the patches of the delay time. Indeed, we observe high values of TD above the mantle wedge and over the backarc region, with time delays up to 2.5 s. Lower values of TD are found in the foreland region.

DISCUSSION

The possibility to have a direct 3-D imaging of the anisotropic structure over geometrically complex systems such as subduction zones could provide constraints on the distribution of deformation and heterogeneities of the mantle and subducting plates at different depths, which in turns help to better understand the mechanisms of

Downloaded from https://academic.oup.com/gji/article/235/2/1725/7257552 by University of Padua: Biblioteca sc. statistiche user on 05 September 2023

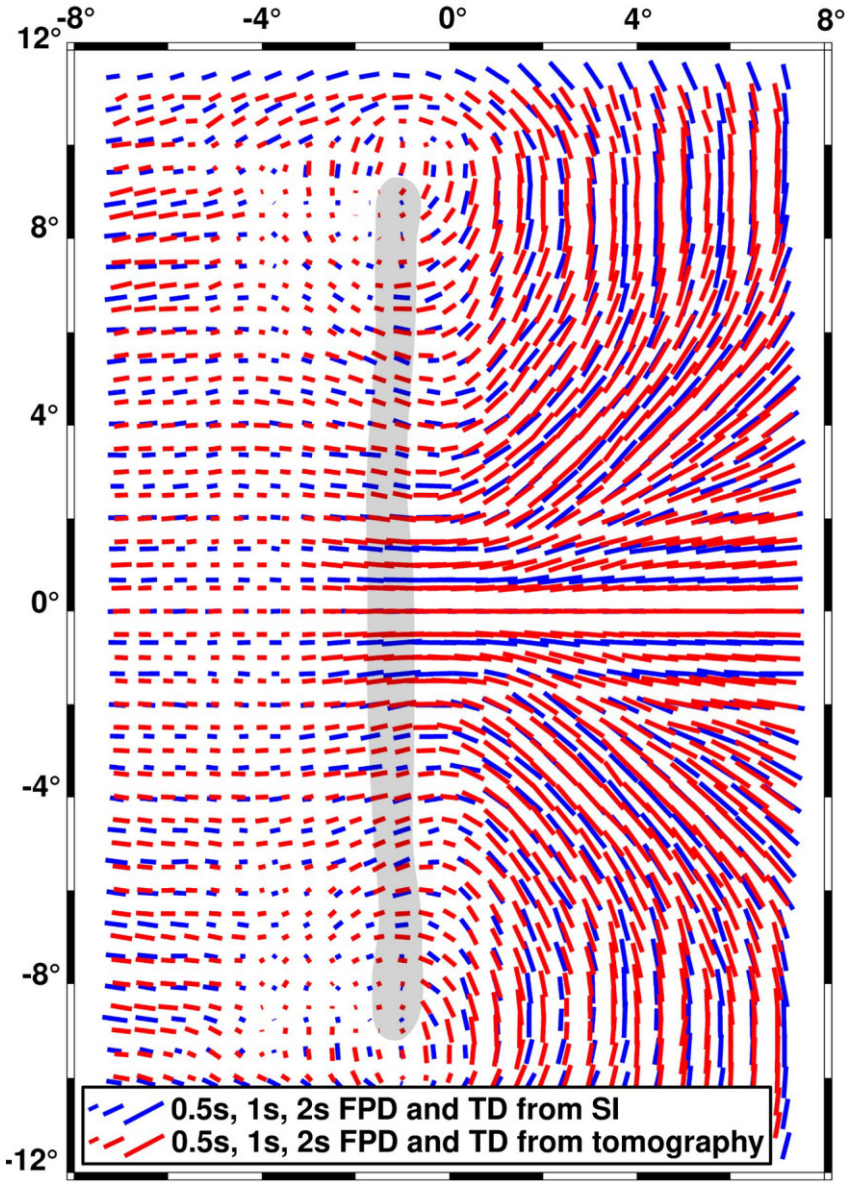

Figure 7. Direct comparison of both shear wave splitting measurements with the grey transparent shape representing the outline of the slab at 150 km depth (Fig. 1a). Marked with red are the splitting parameters restored from the optimal depth dependent shear wave anisotropy model shown in Fig. 5 within the grid of the model. In blue are the splitting parameters from sinusoidal curve fitting (Fig. 2) at each station.

mantle dynamics and lithospheric deformation. Having the opportunity of a realistic model of a subduction system, we tested what SI measurements and their inversion could add to the understanding of the distribution of anisotropy, with respect to a more common core phase shear wave splitting analysis.

SI measurements have been calculated using a modified routine with respect to previous studies, with some adapted criteria to guarantee the good quality of results and automatized the procedure to process data in a large study region and with a huge amount of waveforms. This allowed us to calculate splitting parameters similar to the average shear wave splitting results (VanderBeek & Faccenda 2021).

By applying the 360° fitting sinusoidal curves, this study has also proven that the δt_2 parameter could be a one dimensional indicator for the presence of dipping anisotropy in a regional model. In the slab region clearly a big disagreement of the 180° sinusoid curves and a better fit obtained with the 360° curves can be interpreted as a detection of the presence of dipping anisotropy. At the same time below the slab low δt_2 values support the absence of dipping structures. The backarc region and the edges of the slab are complicated and do not show a δt_2 pattern easy to be interpreted, even if strong variations indicate that anisotropy is not simply horizontal. This method has been previously applied only on simple 'one layer' models. To show a significant δt_2 variations, a dip larger than 30° (Chevrot 2000) and smaller than about 60° with strongly anisotropic material is needed, as well as a good azimuthal coverage of the events and high quality waveforms, since the sinusoidal fitting is very sensible. Therefore, the test described here, the first one on a very complex model, shows the possibility to identify the presence of dipping anisotropy and to confirm that maximum values of δt_2 may be related to 30–60 degrees of dipping. On the contrary it seems really difficult to detect quasi vertical anisotropy;

Downloaded from https://academic.oup.com/gji/article/235/2/1725/7257552 by University of Padua: Biblioteca sc. statistiche user on 05 September 2023

indeed, at 0°N, above the slab, between 6°E and 8°E, where a lower layer shows a nearly 90° dipping, δt_2 is close to zero. Furthermore, according to Chevrot *et al.* (2004), the sinusoidal symmetry can be slightly broken for incidence angles of 10° and higher, instead of vertical, which is a typical incidence angle for SKS waves. In this study our incidence angles only vary between 4° and 8° (Fig. S3), but this fact should be taken into account when working with real data and a greater span of incidence angles.

All SI measurements have been inverted to obtain the tomographic images in Fig. 5. With respect to traditional seismic anisotropy studies, the tomography seems to reveal the distribution of the horizontal anisotropy with depth in different parts of the subduction system, comparable with the model for which this distribution is known (Figs 5 and S1).

First, it is evident that the intensity of the anisotropy shows maximum values in front of the slab and where toroidal flows develop toward the slab edges at intermediate depths (100–150 km). This is very similar to the model anisotropy pattern (Figs 1 and S1). The strong anisotropy of the upper layers (e.g. at 50 and 70 km depths) including the slab (Figs S1 and S2), can not be reproduced with the inversion of SI, due to the small vertical resolution close to the surface, as well as to vertical smearing (Fig. S3). The same can be said for the recovery of strong dipping anisotropy in the thin slab in deeper layers, prevented also by the fact that the inversion is performed for horizontal anisotropy only. Reaching a depth of 350 km, the strength of anisotropy declines, similar to the model anisotropy (Figs 5 and S1). The strength of the anisotropy below the slab is recovered well at depth (below 150 km depth). However, the change of direction can not be recovered, since the two perpendicular oriented anisotropy patterns cancel each other out.

Focusing on the anisotropy direction pattern, the recovery is very good again in front of the slab, with a good reproduction of the horizontal toroidal flows more and more pervasive with depth. Also, some small changes in the anisotropy direction occurring in the central part of the dipping slab (e.g. 300 km slice, latitude 0°, longitude 4° of the model, Fig. S1) are visible in the tomographic images. However, some parts of the model, mainly dipping structures, are not recovered by the tomography, because we are able to invert only for horizontal anisotropy. Yet the pattern shown in Fig. 5 and the evident changes with depth, as concerns anisotropy direction as well as its strength, demonstrate the larger amount of features that SI inversion makes available. In addition the δt_2 measurements allow us to hypothesize where at depth dipping anisotropy may be present and add this information in the interpretation.

Compared to studies based on real data, the distribution of back-azimuths is ideal here, even with just eight events, and therefore sinusoidal curve-fitting was easy. Especially δt_2 values might not be easy to recover when dealing with real data. Additionally, most subduction zones have oceans close to them with limited options to install permanent stations and it would be therefore difficult to find such a dense and evenly distributed station network. On the other hand, a wider range of incidence angles, when including more epicentral distances, could improve depth dependent anisotropy inversion results.

CONCLUSION

We tested SI measurements inversion on data from a synthetic model of a subduction zone, for which the 3-D distribution of the anisotropy is well known. The greatest limit of shear wave seismic anisotropy measurements is the vertical resolution. SI measurements have been done on synthetic waveforms recorded by 770 stations located over a regular grid. The SI values have been then inverted obtaining an anisotropy tomography to be compared with the starting model. The recovery shows a very good quality concerning the strength as well as the direction pattern. Most of the main relevant features for a subduction zone are reconstructed, as for instance the very well visible circular flow around the slab edges or the strongest intensity values in the mantle wedge. The structures that are not in the final tomographic 3-D images are those characterized by dipping anisotropy (e.g. the thin dipping frozen anisotropy in the slab), since the inversion restores horizontal anisotropy only. However, there are parameters from SI measurements that describe the possible presence of dipping anisotropy, that is the average δt_2 by mapping which, together with tomographic images, allow to identify locations of dipping structures. We then consider the results of this test convincing of the improving knowledge that SI measurements inversion may return, when applied on complex geodynamic systems.

ACKNOWLEDGMENTS

We would like to thank one anonymous reviewer and Sebastien Chevrot for their very helpful comments during the revision. Additionally we would also like to give our appreciation to the editor Huajian Yao. Some of the authors have been funded by the NEWTON (NEw Window inTO Earth's iNterior), ERC StG funded project (grant ID:758199) and in the frame of the project INGV Pianeta Dinamico 2021–2022 Tema 4 KINDLE (grant no. CUP D53J19000170001) funded by the Italian Ministry of University and Research 'Fondo finalizzato al rilancio degli investimenti delle amministrazioni centrali dello Stato e allo sviluppo del Paese, legge 145/2018″.

DATA AVAILABILITY

SI measurements as well as the inversion results can be found at: https://osf.io/hdx2v/?view_only=0b0856cc17b0444f89cce15d3bd9f76f. The initial anisotropic model is published by VanderBeek & Faccenda (2021). Links to the model can be found in their supporting material.

REFERENCES

Becker, T.W., Chevrot, S., Schulte-Pelkum, V. & Blackman, D.K. 2006. Statistical properties of seismic anisotropy predicted by upper mantle geodynamic models, *J. geophys. Res.,* **111**(B8), doi:10.1029/2005JB004095.

Beller, S. & Chevrot, S. 2020. Probing depth and lateral variations of upper-mantle seismic anisotropy from full-waveform inversion of teleseismic body-waves, *Geophys. J. Int.,* **222**(1), 352–387.

Bezada, M.J., Faccenda, M. & Toomey, D.R. 2016. Representing anisotropic subduction zones with isotropic velocity models: a characterization of the problem and some steps on a possible path forward, *Geochem. Geophys. Geosyst.,* **17**(8), 3164–3189.

Chevrot, S. 2000. Multichannel analysis of shear wave splitting, *J. geophys. Res.,* **105**(B9), 21 579–21 590.

Chevrot, S. 2006. Finite-frequency vectorial tomography: a new method for high-resolution imaging of upper mantle anisotropy, *Geophys. J. Int.,* **165**(2), 641–657.

Chevrot, S., Favier, N. & Komatitsch, D. 2004. Shear wave splitting in three-dimensional anisotropic media, *Geophys. J. Int.,* **159**(2), 711–720.

Downloaded from https://academic.oup.com/gji/article/235/2/1725/7257552 by University of Padua: Biblioteca sc. statistiche user on 05 September 2023

Chevrot, S. & Van Der Hilst, R.D. 2003. On the effects of a dipping axis of symmetry on shear wave splitting measurements in a transversely isotropic medium, *Geophys. J. Int.,* **152**(2), 497–505.

Confal, J.M., Bezada, M.J., Eken, T., Faccenda, M., Saygin, E. & Taymaz, T. 2020. Influence of upper mantle anisotropy on isotropic P-wave tomography images obtained in the Eastern Mediterranean region, *J. geophys. Res.,* **125**(8), e2019JB018559, doi:10.1029/2019JB018559.

Confal, J.M., Faccenda, M., Eken, T. & Taymaz, T. 2018. Numerical simulation of 3-D mantle flow evolution in subduction zone environments in relation to seismic anisotropy beneath the eastern Mediterranean region. *Earth planet. Sci. Lett.,* **497,** 50–61.

Diaz, J., Gil, A. & Gallart, J. 2013. Uppermost mantle seismic velocity and anisotropy in the Euro-Mediterranean region from Pn and Sn tomography, *Geophys. J. Int.,*(2013),**192,** 310–325.

Eberhart-Phillips, D. & Reyners, M. 2009. Three-dimensional distribution of seismic anisotropy in the Hikurangi subduction zone beneath the central North Island, New Zealand, *J. geophys. Res.,* **114**(B6),.

Efron, B. & Tibshirani, R. 1986. Bootstrap methods for standard errors, confidence intervals, and other measures of statistical accuracy, *Stat. Sci.,* **1**(1), 54–75.

Faccenda, M. 2014. Mid mantle seismic anisotropy around subduction zones, *Phys. Earth planet. Inter.,* **227,** 1–19.

Faccenda, M. & Capitanio, F.A. 2013. Seismic anisotropy around subduction zones: insights from three-dimensional modeling of upper mantle deformation and SKS splitting calculations, *Geochem. Geophys. Geosyst.,* **14**(1), 243–262.

Favier, N. & Chevrot, S. 2003. Sensitivity kernels for shear wave splitting in transverse isotropic media, *Geophys. J. Int.,* **153**(1), 213–228.

Fry, B., Deschamps, F., Kissling, E., Stehly, L. & Giardini, D., 2010. Layered azimuthal anisotropy of Rayleigh wave phase velocities in the European Alpine lithosphere inferred from ambient noise, *Earth planet. Sci. Lett.,* **297**(1–2), 95–102.

Goldstein, P.A.U.L. & Snoke, A. 2005. SAC availability for the IRIS community, *Incorporat. Res. Instit. Seismol. Newslett.,* **7**(1), UCRL-JRNL-211140.

Hansen, P.C. 1992. Analysis of discrete ill-posed problems by means of the L-curve, *SIAM Rev.,* **34**(4), 561–580.

Hearn, T.M. 1996. Anisotropic Pn tomography in the western United States, *J. geophys. Res.,* **101**(B4), 8403–8414.

Huang, Z. & Chevrot, S. 2021. Mantle dynamics in the SE Tibetan Plateau revealed by teleseismic shear-wave splitting analysis, *Phys. Earth planet. Inter.,* **313,** doi:10.1016/j.pepi.2021.106687.

Kaminski, E., Ribe, N.M. & Browaeys, J.T. 2004. D-Rex, a program for calculation of seismic anisotropy due to crystal lattice preferred orientation in the convective upper mantle, *Geophys. J. Int.,* **158**(2), 744–752.

Kennett, B.L.N. & Engdahl, E.R. 1991. Traveltimes for global earthquake location and phase identification, *Geophys. J. Int.,* **105**(2), 429–465.

Kong, F., Gao, S.S. & Liu, K.H. 2015. Applicability of the multiple-event stacking technique for shear-wave splitting analysis, *Bull. seism. Soc. Am.,* **105**(6), 3156–3166.

Kustowski, B., Ekström, G. & Dziewoński, A.M. 2008, Anisotropic shear-wave velocity structure of the Earth's mantle: a global model, *J. geophys. Res.,* **113**(B6), doi:10.1029/2007JB005169.

Lin, Y.-P., Zhao, L. & Hung, S.-H. 2014a, Full-wave effects on shear wave splitting, *Geophys. Res. Lett.,* **41,** 799–804.

Lin, Y.-P., Zhao, L. & Hung, S.-H. 2014b, Full-wave multiscale anisotropy tomography in Southern California, *Geophys. Res. Lett.,* **41,** 8809–8817.

Long, M.D. & Silver, P.G. 2009. Shear wave splitting and mantle anisotropy: measurements, interpretations, and new directions, *Surv. Geophys.,* **30**(4), 407–461.

Mondal, P. & Long, M.D. 2019. A model space search approach to finite-frequency SKS splitting intensity tomography in a reduced parameter space, *Geophys. J. Int.,* **217**(1), 238–256.

Montagner, J.P. 2002. Upper mantle low anisotropy channels below the Pacific Plate, *Earth planet. Sci. Lett.,* **202**(2), 263–274.

Monteiller, V. & Chevrot, S. 2010. How to make robust splitting measurements for single-station analysis and three-dimensional imaging of seismic anisotropy, *Geophys. J. Int.,* **182**(1), 311–328.

Monteiller, V. & Chevrot, S. 2011. High-resolution imaging of the deep anisotropic structure of the San Andreas Fault system beneath southern California, *Geophys. J. Int.,* **186**(2), 418–446.

O'Driscoll, L.J., Humphreys, E.D. & Schmandt, B. 2011. Time corrections to teleseismic P delays derived from SKS splitting parameters and implications for western US P-wave tomography, *Geophys. Res. Lett.,* **38**(19), doi:10.1029/2011GL049031.

Rappisi, F., VanderBeek, B.P., Faccenda, M., Morelli, A. & Molinari, I. 2022. Slab geometry and upper mantle flow patterns in the Central Mediterranean from 3D anisotropic P-wave tomography, *J. geophys. Res.,* **127,** e2021JB023488, doi:10.1029/2021JB023488.

Romanowicz, B. & Yuan, H. 2012. On the interpretation of SKS splitting measurements in the presence of several layers of anisotropy, *Geophys. J. Int.,* **188**(3), 1129–1140.

Saltzer, R.L., Gaherty, J.B. & Jordan, T.H. 2000. How are vertical shear wave splitting measurements affected by variations in the orientation of azimuthal anisotropy with depth?. *Geophys. J. Int.,* **141**(2), 374–390.

Savage, M.K. 1999. Seismic anisotropy and mantle deformation: what have we learned from shear wave splitting?, *Rev. Geophys.,* **37**(1), 65–106.

Silver, P.G. & Chan, W.W. 1991. Shear wave splitting and subcontinental mantle deformation, *J. geophys. Res.,* **96**(B10), 16 429–16 454.

Silver, P.G. & Long, M.D. 2011. The non-commutivity of shear wave splitting operators at low frequencies and implications for anisotropy tomography, *Geophys. J. Int.,* **184**(3), 1415–1427.

Silver, P.G. & Savage, M.K. 1994. The interpretation of shear-wave splitting parameters in the presence of two anisotropic layers, *Geophys. J. Int.,* **119**(3), 949–963.

VanderBeek, B.P. & Faccenda, M. 2021. Imaging upper mantle anisotropy with teleseismic P-wave delays: insights from tomographic reconstructions of subduction simulations, *Geophys. J. Int.,* **225**(3), 2097–2119.

Wang, J. & Zhao, D. 2013. P-wave tomography for 3-D radial and azimuthal anisotropy of Tohoku and Kyushu subduction zones, *Geophys. J. Int.,* **193**(3), 1166–1181.

Wei, W., Zhao, D., Wei, F., Bai, X. & Xu, J. 2019. Mantle dynamics of the eastern Mediterranean and Middle East: constraints from P-wave anisotropic tomography, *Geochem. Geophys. Geosyst.,* **20**(10), 4505–4530.

Zhu, H., Bozdağ, E. & Tromp, J. 2015. Seismic structure of the European upper mantle based on adjoint tomography, *Geophys. J. Int.,* **201**(1), 18–52.

SUPPORTING INFORMATION

Supplementary data are available at *GJIRAS* online.

Figure S1. Horizontal cross-sections (50–350 km depths) of the true azimuthal anisotropy.

Figure S2. Vertical cross-sections (10°–0°N) of the true anisotropy.

Figure S3. Example seismograms of the eight events at station SYN377 with P- and SKS-wave arrivals marked in blue and red respectively on the transverse component.

Figure S4. On the left-hand side, the amount of waveforms for each 0.1° of incidence angle are shown with an inset of the backazimuthal distribution of the used events. On the right-hand side, the incidence angles for the six stations which are also highlighted in Figs 2 and 3, are shown in different colours and symbols.

Figure S5. Vertical cross-sections (5°–0°N) of the model anisotropy.

Please note: Oxford University Press is not responsible for the content or functionality of any supporting materials supplied by the authors. Any queries (other than missing material) should be directed to the corresponding author for the paper.

© The Author(s) 2023. Published by Oxford University Press on behalf of The Royal Astronomical Society. This is an Open Access article distributed under the terms of the Creative Commons Attribution License (http://creativecommons.org/licenses/by/4.0/), which permits unrestricted reuse, distribution, and reproduction in any medium, provided the original work is properly cited.

Downloaded from https://academic.oup.com/gji/article/235/2/1725/7257552 by University of Padua: Biblioteca sc. statistiche user on 05 September 2023